INDONESIAN JOURNAL ON GEOSCIENCE
Geological Agency
Ministry of Energy and Mineral Resources

Journal homepage: https://ijog.geologi.esdm.go.id
ISSN 2355-9314, e-ISSN 2355-9306

Advanced Satellite-Based Spectral Techniques for Identifying and Quantifying Soil Clay Minerals

Rina Devnita, Ilmi Ramadhan, and Mahfud Arifin

Department of Soil Science and Land Resources, Faculty of Agriculture,
Universitas Padjadjaran, Jatinangor-Sumedang, Indonesia

Corresponding author: rina.devnita@unpad.ac.id
Manuscript received: March, 21, 2025; revised: July, 23, 2025;
approved: August, 25, 2025; available online: August, 29, 2025

Abstract - Soil mineral plays an important role in agriculture due to its ability in influencing soil physical and chemical characteristics, and therefore is important to be identified. The techniques for identifying soil minerals, such as the utilization of a polarization microscope and X-Ray Diffraction (XRD), are often laborious, time-consuming, and costly. This study aims to identify and to quantify soil clay minerals by using Hyperion EO-1 imagery and XRD methods, and to reveal the effectiveness of using satellite imagery to determine soil minerals. Spectral signatures from Hyperion EO-1 were extracted in alignment with the soil sampling coordinate locations, and spectral data processing methods such as Continuum Removal (CR), and Savitzky-Golay filtering were used to identify and to quantify minerals. The results show that hyperspectral analysis revealed distinct spectral absorption features, and it could identify kaolinite, chlorite, goethite, hematite, and plagioclase. Meanwhile, XRD analysis confirmed kaolinite and chlorite, consistent with the hyperspectral observations. A key advantage of the spectral absorption technique for raw soil was its ability to identify not only clay minerals, but also both primary and secondary minerals; such as plagioclase, hematite, and goethite, that remain unidentified when using the XRD method with iron removal pre-treatment. Although hyperspectral imagery was successful in identifying soil minerals, there are still some limitations that require further refinement, especially while conducting quantification. The findings underscored the potential of satellite-based hyperspectral analysis as a rapid alternative approach to soil mineral identification that can reduce reliance on laboratory-based methods.

Keywords: remote sensing, hyperspectral imaging, clay identification, soil reflectance, spectral absorption

How to cite this article:
Devnita, R., Ramadhan, I., and Arifin, M., 2025. Advanced Satellite-Based Spectral Techniques for Identifying and Quantifying Soil Clay Minerals. *Indonesian Journal on Geoscience*, 12 (2), p.301-318. DOI: 10.17014/ijog.12.2.301-318

Introduction

Clay minerals play a fundamental role in shaping various soil properties. Several characteristics of soils that are influenced by clay minerals include cation exchange capacity (CEC), water retention, water availability, structural stability, bulk density, and porosity (Kome *et al.*, 2019). As a key reactive components in soil systems, clay minerals influence critical biogeochemical processes, plant growth, and soil aggregation (Zhang *et al.*, 2021). Given their significant role in soil function and plant productivity, accurate identification and characterization of clay minerals are essential for effective soil management and sustainable agriculture.

Mineral analysis is a crucial step in identifying soil clay minerals. Bhat *et al.* (2024) highlighted

the importance of analysing soil clay minerals for making informed agricultural management decisions. One of the most widely used techniques for clay mineral identification is X-Ray Diffraction (XRD), which was first introduced for soil clay mineral analysis in 1930 (Hendricks and Fry, 1930; Churchman, 2018). The XRD analysis remains a powerful analytical tool to identify clay minerals (Xiao *et al*., 2023). However, it involves a labour-intensive, multi-step processes including raw soil sample preparation, clay particle extraction, removal of iron oxides, and XRD scanning to generate the results (McAlister and Smith 1995).

In recent decades, researchers have been exploring more efficient methodologies, leveraging statistical approaches and artificial intelligence (AI) to improve clay mineral analysis. The application of machine learning has seen significant advancements, allowing for the development of predictive models that enhance mineral identification accuracy (He *et al*. 2024). Additionally, satellite imagery and remote sensing technologies have become increasingly prominent in soil research, offering a faster and more cost-effective alternative for large-scale mineral analysis.

Remote sensing techniques provide an innovative and efficient approach for mapping and identifying clay minerals. Altinbas *et al*. (2005) demonstrated that advanced remote sensing technologies, such as spectral analysis, enable identification of clay minerals to be cost-effective. These methods utilize sensors on satellites, aircraft, or drones to collect spectral data, facilitating large-scale soil property assessments, even in remote or inaccessible regions (Bellinaso *et al*., 2021). Demattê *et al*. (2016) emphasized that remote sensing-derived data can be analyzed for multiple purposes, including soil mineral identification and moisture assessment. High spatial and spectral resolution imagery enhances the precision of soil property mapping, enabling extensive agricultural areas to be effectively monitored (Garfagnoli *et al*., 2013). Additionally, Ben-Dor (2002) highlighted that remote sensing allowed for temporal monitoring of soil properties.

In particular, hyperspectral remote sensing has shown significant potential for mapping and discriminating clay minerals based on their spectral absorption features in the Short Wave Infrared Region (SWIR) . However, most applications of this technology have focused on geological formations, arid zones, or mining regions, rather than agricultural soils. Several studies using multispectral sensors such as Landsat, ASTER, or Sentinel-2 have attempted to map clay content, but these sensors lack the spectral resolution for distinguishing specific mineral types. For example, ASTER could detect clay-enriched zones, but failed to quantify montmorillonite content below 16 %, and Sentinel-2 showed only moderate performance when scaled beyond local calibrations (Ducasse *et al*., 2024).

More promising results have emerged from AVIRIS-NG or AISA-FENIX—which successfully mapped kaolinite, montmorillonite, and illite with reasonable accuracy ($R^2 \approx 0.62$ - 0.70) in Brazil and India (Priya and Ghosh, 2022; Nanni *et al*., 2021). However, these studies are highly site-specific, often conducted over bare or homogeneous soils, and remain rare in humid tropical agricultural environments, particularly plantations. Moreover, satellite-based hyperspectral platforms such as Hyperion EO-1 or PRISMA are still underutilized in this context. Although capable of detecting key clay minerals, their relatively coarse spatial resolution (30 m) and low signal-to-noise ratio result in mixed pixels that reduce spectral clarity, especially problem in vegetated or heterogeneous farm landscapes.

A further gap exists in the quantification and validation of clay minerals using remote sensing. While continuum-removal and spectral unmixing algorithms are available, their application to soils that are often rich in organic matter and moisture remains underexplored. Even where clay abundance maps have been generated, few studies rigorously validate them against laboratory data. Additionally, although proximal sensing methods (*e.g*. Vis–NIR, pXRF) have shown some promise in mineral quantification, quantitative models for specific clay types are still limited and often confined to small, laboratory-based datasets.

In this study, the application of Hyperion EO-1 was focused on clay mineral identification

and quantification in a tea plantation located in Lembang District, West Java Province, Indonesia. This plantation spans approximately 231 ha, and is situated at an altitude range of 1,323 to 1,813 m above sea level. Although extensive soil characteristic data exists for this area, remote sensing-based mineral composition analysis has not been conducted. The studied site was selected due to its homogeneity in key environmental factors, including vegetation (tea plantation), climate (Agroclimatic Zone A), parent materials (sandy tuff), and sloping topography. Understanding mineral composition through remote sensing will aid plantation management in making informed decisions to optimize soil treatment and enhance tea production. By utilizing remote sensing techniques, this study aims to provide soil clay mineral data from satellite-based analysis for the alternative to laborious and time-consuming techniques.

Data and Methods

Studied Area

The study was conducted at a tea plantation area located on the southwestern slope of Tangkuban Parahu Volcano (Figure 1). This area was selected due to homogeneous land use (*i.e.* tea plantation) which can minimize deterioration of soil texture determination and clay mineral identification caused by various soil managements applied to them (Figure 2). Based on the soil type map on a semidetailed scale (1:50,000)

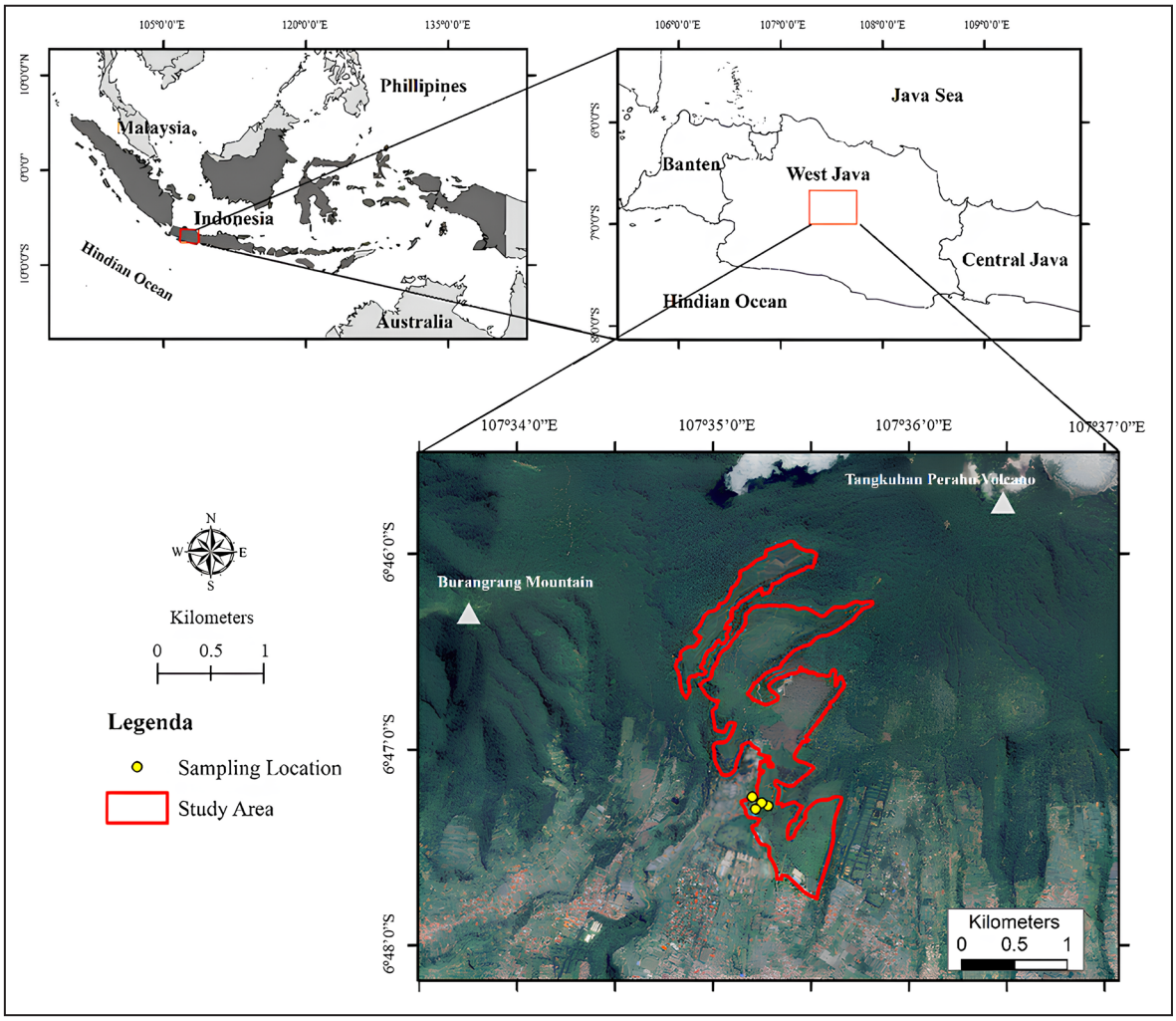

Figure 1. Map of the study of location.

Figure 2 Present field conditions of tea plantation cover in the studied area.

from Indonesian Centre for Agriculture Land Resources (CALR) (Sukarman *et al*., 2016), the studied area has been known to have two different soil order namely Entisols and Andisols. Andisols covered 38.82 % of the total area, whereas Entisols covered 61.18 %. Both soil orders was developed from weathering processes of several volcanic materials including pumiceous tuff (Qyt), lava (Qyl), and sandy tuff (Qyd) based on the geological map from Silitonga (1973) (Figure 1). Rainfall in the studied area falls into "A" agroclimatic zone according Oldeman (1973) with the average annual precipitation of 2978.77 mm/year, consisting of eight wet months without any dry month observed.

Data Acquisition

The Hyperion EO-1 hyperspectral imagery, developed by NASA, was selected for this study due to its capability to capture a broad spectrum range from the visible-near infrared (400 - 1,000 nm) to the shortwave infrared (900 - 2,500 nm) (Pearlman *et al*., 2001). This imagery has 30 m of spatial resolution. The image date for this research is from acquisition conducted on September 12nd, 2012, during the transition between the dry and wet seasons, based on optimal cloud coverage and the availability for the studied area. A total of sixty-six bands were excluded due to low sensitivity, band overlap, baseline noise, and atmospheric water vapour absorption. The remaining bands were processed using a stripping algorithm to correct pixel noise, followed by radiometric corrections to convert at-sensor radiance into surface reflectance. Atmospheric correction was conducted using The Fast Line-of-sight Atmospheric Analysis of Spectral Hypercube (FLAASH) Algorithm in ENVI 5.3 software. Figure 3a displays The Google Imagery for general land cover reference, while Figure 3b shows the EO-1 Hyperion image used in this study, highlighting the selected bare soil pixels for analysis.

Methodology

The methodology of this study comprised several stages, including Hyperion EO-1 image selection, soil sampling, laboratory soil analysis, and mineral identification. Initially, the appropriate Hyperion EO-1 satellite imagery was selected based on factors such as cloud cover, image quality, and suitability for spectral analysis. Subsequently, soil sampling was conducted following a systematic approach to ensure representative data collection across the studied area.

Once collected, the soil samples underwent laboratory analysis to determine their texture classification, which served as a basis for mineralogical analysis. The identified soil texture classes were then utilized to extract spectral reflectance data from the Hyperion EO-1 imagery. This spectral information was analyzed to identify and to quantify the clay minerals present in the soil. The overall workflow of the soil mineral identification process, including the integration of remote sensing data and laboratory analysis, is depicted in Figure 4.

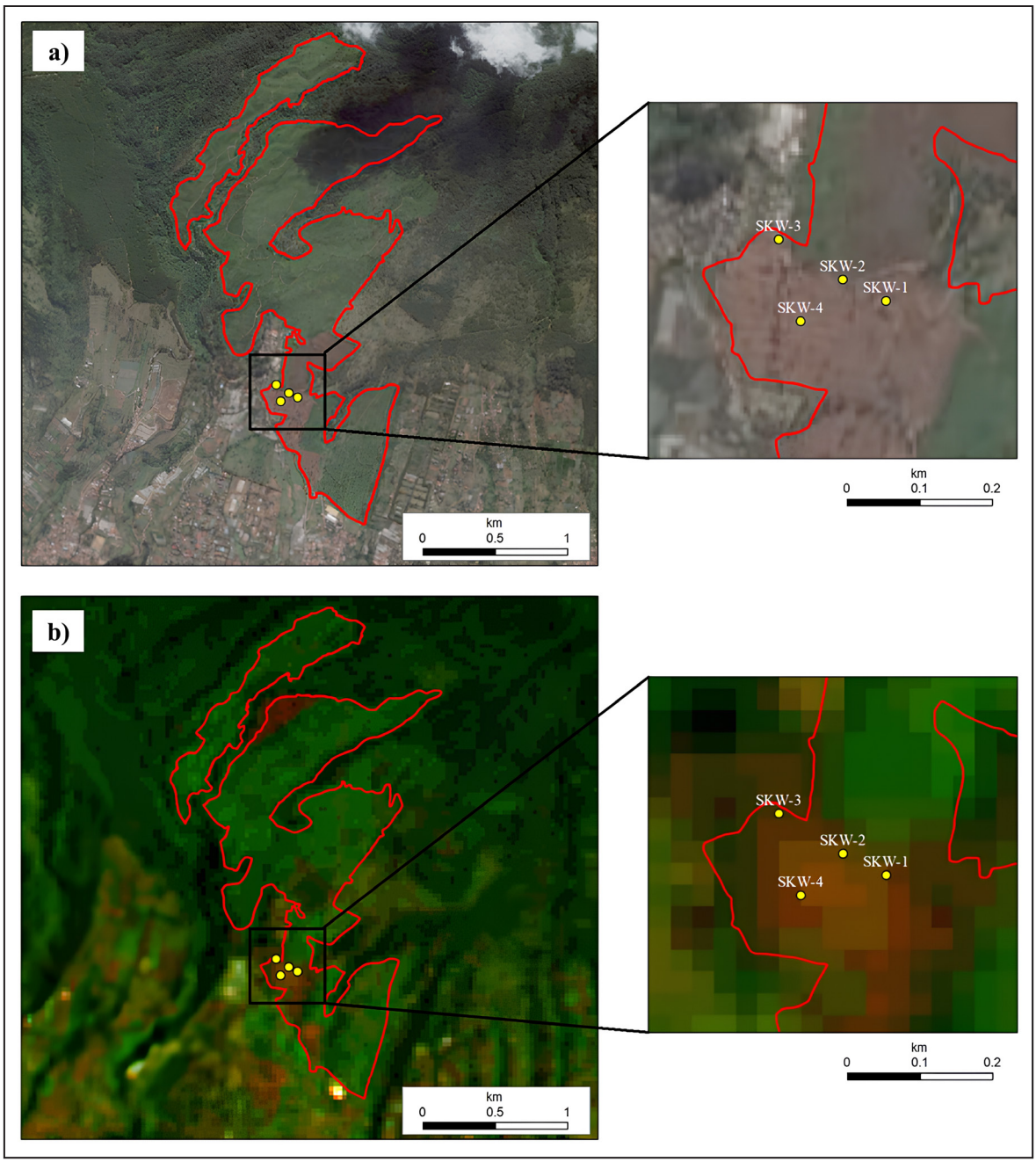

Figure 3. Selected pixel locations for spectral extraction over bare soil areas within a tea plantation, as observed in (a) Google Imagery and (b) Hyperion EO-1 imagery in true colour, both dated September, 2012.

Soil Sampling Method

The soil sampling aims to collect soil from the field, for further analysis in the laboratory to identify the soil texture, to collect the clay extraction, and to analyze the mineral with XRD. In this study, soil sampling was conducted based on covariate space and coverage sampling methods (Brus, 2019). Determination of sampling points was done using the k-means clustering algorithm applied to Hyperion EO-1 satellite imagery resulted in four soil sampling locations. This method involved segmenting the image pixels into clusters that reflect similarities in vegetation cover, topography, climate conditions, and parent material age. The k-means clustering approach enables the identification of representative sampling locations by grouping pixels with similar spectral characteristics, thereby improving the efficiency

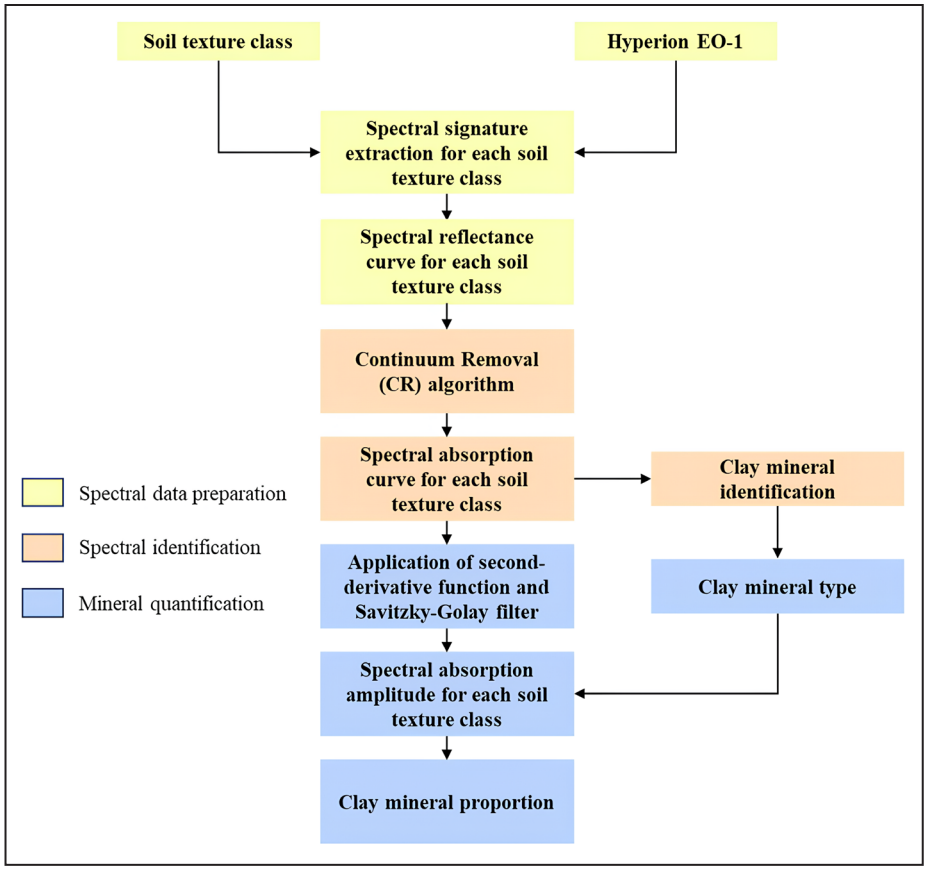

Figure 4. Flow diagram of methodology in this study.

and accuracy of soil sampling. Once the sampling points were identified, soil samples were collected at each location and subjected to laboratory analysis for mineral composition. However, the relatively small number of sampling locations may limit the ability to capture the full variability of soil properties across the studied area. The spectral signatures obtained from Hyperion EO-1 were analyzed to determine the dominant clay minerals present are within the studied area.

Soil Analysis

Soil Textural Determination

The process of determining soil texture involved quantifying the proportions of sand, silt, and clay particles, each of which contributes to the overall composition of the soil. First, 20 g sample of field-moist soil was sieved to remove particles larger than 2 mm, as maintaining the soil natural moisture helps preserve its structural integrity (Poulenard *et al*., 2003). To break down the organic matter present in the soil, hydrogen peroxide (H_2O_2) was added to the sample, which was then heated in a water bath at 100°C until the reaction ceased *(Kitagawa et al.*, 2004). Afterward, sodium pyrophosphate ($Na_4P_2O_7$) at a concentration of 0.04 M was introduced to facilitate particle dispersion. The sand fraction (0.05–2.00 mm) then was separated by using wet sieving, while the finer silt (0.002–0.05 mm) and clay (<0.002 mm) fractions were isolated through the Köhn pipette technique. Finally, the dry weight of each fraction was measured, allowing for the calculation of the relative proportions of sand, silt, and clay to provide a complete picture of the soil textural composition.

Clay Extraction Technique

Clay fraction separation was performed on soil samples with silty clay and silty clay loam using a combination of wet sieving, gravity sedimentation, and centrifugation techniques, following

the method described by Xing and Dudas (1994). Soil samples from two different textures were chosen due to their clay proportion. The soil aggregate dispersion process was carried out using distilled water and a 0.04M sodium pyrophosphate ($Na_4P_2O_7$) solution in a 1,000 ml graduated cylinder, followed by an incubation period of 6.5 hours. The fine clay fraction was then separated from the suspension.

To eliminate iron oxide content from the fine clay fraction, the samples were treated with sodium dithionite solution supplemented with citrate-bicarbonate, a method commonly employed for iron oxide removal (Uzarowicz *et al*., 2011). The final separation step involved centrifugation, where the fine clay fraction was spun at 5,000 revolutions per minute for 20 minutes to ensure effective isolation of clay particles for further mineralogical analysis.

Mineralogical Analyses

Clay Mineral Identification using Hyperion EO-1 Spectral Response

The pixels in the Hyperion EO-1 hyperspectral image which reflects four soil textures were extracted and converted into spectral reflectance data to facilitate further analysis. This process involved calibrating the raw at-sensor radiance values to surface reflectance, ensuring the spectral measurements accurately represented the inherent properties of the soil. The four reflectances representing each sample location were then averaged based on their texture class similarity. Absorption characteristics of the soil minerals were analyzed using extracted reflectance data that previously had been calculated from the absorbance values of each corresponding pixel.

The spectral response of soil samples was analyzed following soil texture classification. The spectral reflectance corresponding to each soil texture class was extracted to facilitate clay mineral identification. Continuum Removal (CR) function was employed to normalize reflectance spectra, enabling the comparison of absorption properties against a baseline (Wadoux *et al*., 2021). A continuum removal spectra is a convex line fitted over a spectrum reflectance curve, connecting its maximum values through straight-line segments. Two methods that can normalize the spectrum are: additive and division (Clark and Roush, 1984). The additive technique maintains a constant depth of the spectral absorption curve across the wavelength range. CR assigns a value of 0 to all spectral regions on the convex hull and values between 0 and 1 within absorption bands (Wadoux *et al*., 2021). Essentially, CR enhances spectral absorption bands by minimizing brightness variations (Buddenbaum and Steffens, 2012). The CR algorithm was applied using the Continuum Removal function in the R 4.2.1 prospect package. Clay mineral identification was subsequently conducted by comparing spectral absorption features at specific wavelengths with referenced spectra from The United States Geological Survey (USGS) Spectral Library Version 7 (Kokaly *et al*., 2017) and soil mineral spectroscopy studies (*e.g.* Abweny *et al*., 2016). Basically, CR algorithm is derived from the equation x below:

$$S_{CR} = \frac{S}{C} \quad \text{.....(1)}$$

where:

S_{CR} is continuum-removed spectra,

S is original reflectance, and

C is baseline continuum envelope fitted over the spectrum.

The second derivative function was applied to the reflectance curve of the continuum-removed spectrum to quantify the energy amplitude of absorption features detected by the sensor (Mendes *et al*., 2021). The amplitude values were then used to estimate the proportion of each clay mineral present. According to Stevens and Ramirez-Lopez (2013), the second derivative function can be applied using two methods: (1) computing the finite difference between consecutive wavelength values, and (2) applying the second derivative function over a smoothed spectrum using the Savitzky-Golay filter (Savitzky and Golay, 1964). The latter approach, which involves deriving

the smoothed spectrum, was implemented using the "SavitzkyGolay" function from the prospect package in R (Wadoux *et al*., 2021). The general form of its equation is:

$$Y_j = \sum_{i=\frac{m-1}{2}}^{\frac{m-1}{2}} C_i \cdot y_{j+1}, \frac{m+1}{2} \leq j \leq \frac{m-1}{2} \quad .....(2)$$

Where:

Yj is smoothed value at index j,

y_j+i is original data points,

C_i is convolution coefficients, and

m is window length in odd numbers.

Clay Mineralogy Using X-Ray Diffraction (XRD)

Clay mineral analysis procedures followed American Standard for Testing Materials (ASTM) No. E3294-22 standard guidelines for forensic analysis of geological materials using X-Ray Diffraction (XRD) (ASTM, 2023). The XRD scanning was performed using a PANalytical X'Pert PRO PW3040/X0 instrument (Malvern Panalytical, UK), equipped with a Hybrid Pixel detector and a Cu-K target metal wavelength of 1.54060 Å. Mineral phase analysis was conducted using Profex XRD 4.3.6 software (Doebelin and Kleeberg, 2015), with diffraction peak matching against databases from Profex XRD and Brindley and Brown (1980).

Results and Discussion

Soil Textural Determination

Table 1 presents the results of the soil texture analysis. The classification indicates two distinct soil texture classes: silty clay and silty clay loam. The highest clay content was observed at site SKW-4 with 44.3 %, followed by SKW-1 (44.26 %), SKW-2 (31.34 %), and SKW-3 (29.94 %). Sites SKW-2 and SKW-3 were found to contain more than 50 % silt, while SKW-1 and SKW-4 had silt content below 50 %. Sand content varied considerably across all four sampling locations, but generally remained below 20 %.

Spectral Reflectance Characteristics for Each Textural Class

Spectral reflectance analysis provides valuable insights into soil texture classification by capturing variations in mineral composition, moisture content, and surface properties. The spectral reflectance characteristics obtained from Hyperion EO-1 imagery reveals distinct differences between soil texture classes. The differences in the average reflectance values across the Visible-Near Infra Red-Shortwave Infra Red (VIS-NIR-SWIR) spectral range for the two identified soil texture classes (*i.e.* silty clay loam and silty clay) are illustrated in Figure 5. The most pronounced

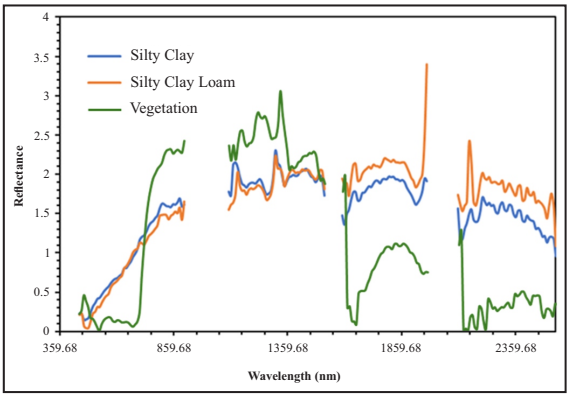

Figure 5. Spectral reflectance indicating higher soil albedo in the silty clay loam texture compared to silty clay in the SWIR spectrum.

Table 1. Results of Soil Texture Analysis at Four Sampling Locations (SKW-1 to SKW-4), Showing The Percentage of Sand, Silt, and Clay, and the Corresponding Soil Texture Classes

Location	Sand	Silt	Clay	Soil Texture Class
	----------%----------			
SKW-1	15.15	40.59	44.26	Silty Clay
SKW-2	17.30	51.36	31.34	Silty Clay Loam
SKW-3	13.83	57.23	28.94	Silty Clay Loam
SKW-4	14.40	41.23	44.38	Silty Clay

spectral reflectance separation occurs in the SWIR region (1599.2–2536.16 nm), where silty clay loam exhibits higher reflectance than silty clay. This increased reflectance in the SWIR spectrum suggests that silty clay loam contains lower moisture content, leading to an enhanced albedo effect, particularly at wavelengths between 1,400 and 1,900 nm (Ben-Dor, 2002). As a comparison, vegetation spectral reflectance characteristic is very distinct from those from soil textures. The vegetated area, in this case tea, have a higher reflectance in NIR region (800–1,200 nm) and low reflectance in SWIR region, whereas soil has the opposite reflectance characteristics.

In contrast, within the VIS-NIR spectrum (400–1,000 nm), silty clay loam generally exhibits lower reflectance than silty clay, except for a noticeable increase between 652.78 and 691.52 nm. These findings align with Pereira *et al.* (2019), who reported that soils with iron content exceeding 120 g kg^{-1} tend to exhibit higher reflectance within the ±600 - 750 nm wavelength range. The variation in reflectance at these wavelengths is strongly influenced by the absorption characteristics of iron oxide minerals, both in crystalline and noncrystalline forms (Fang *et al*., 2018). The presence of water and iron oxides significantly affects the shape and depth of spectral absorption features, ultimately influencing the reflectance properties of different soil textures.

Spectral Absorption Characteristics and Mineral Identification

The spectral reflectance extraction from Hyperion EO-1 imagery was performed on four pixels of silty clay texture and six pixels of silty clay loam. To minimize spectral noise, three representative pixels were selected for each texture class. The continuum removal (CR) curves of both textures reveal distinct spectral absorption features (Figure 6). The spectral patterns of each texture class exhibited varying absorption intensities at different sample points, as indicated by the curve colour differences as can be seen in Figure 6. The differences in absorption intensity are likely due to varying amounts of minerals, organic matter, and water, which create distinct albedo effects.

The spectral absorption patterns of both textures exhibit similarities, with absorption features observed in the VNIR (~470 nm, ~700 nm, ~1,250 nm, ~1,400 nm) and SWIR (~1,500 nm, ~1,600 nm, ~1,900 nm, ~2,100 nm, ~2,300 nm) regions. However, notable differences in the absorption positions and intensities suggest variations in mineralogical composition and crystallinity between the two textures.

Iron Oxides: Hematite and Goethite

Hematite and goethite were identified in both soil textures. The goethite absorption feature at 476.8 nm appears in both silty clay and silty clay loam, while hematite absorption occurs at 740.32 nm in silty clay, but shifts to a shorter wavelength (730.56 nm) in silty clay loam. This shift in hematite absorption can be attributed to differences in charge transfer between ligands (O_2^- or OH^-) and Fe^{3+} ions, as influenced by the electronegativity of the surrounding environment (Elias *et al*., 2006). The shorter absorption wavelength in silty clay loam suggests a more ionic bond between ligands and Fe^{3+}, likely due to variations in redox conditions and soil formation processes.

The sharper and more symmetrical absorption features of both hematite and goethite in silty clay loam indicate a higher degree of crystallinity than in silty clay. This is consistent with findings by Fang *et al.* (2018), who reported that well-crystallized iron oxides exhibit narrower spectral absorption features. The differences in crystallinity are likely linked to oscillating redox conditions, where intermittent anoxic conditions facilitate the reduction and leaching of short-range order iron minerals, leaving behind more crystalline forms (Thompson *et al*., 2006). This phenomenon is further supported by the higher albedo of the silty clay loam texture compared to the silty clay texture, suggesting lower water content and more pronounced redox oscillations in the former. The findings aligned with recent studies emphasizing the influence of soil organic matter on the electron transfer and atom exchange

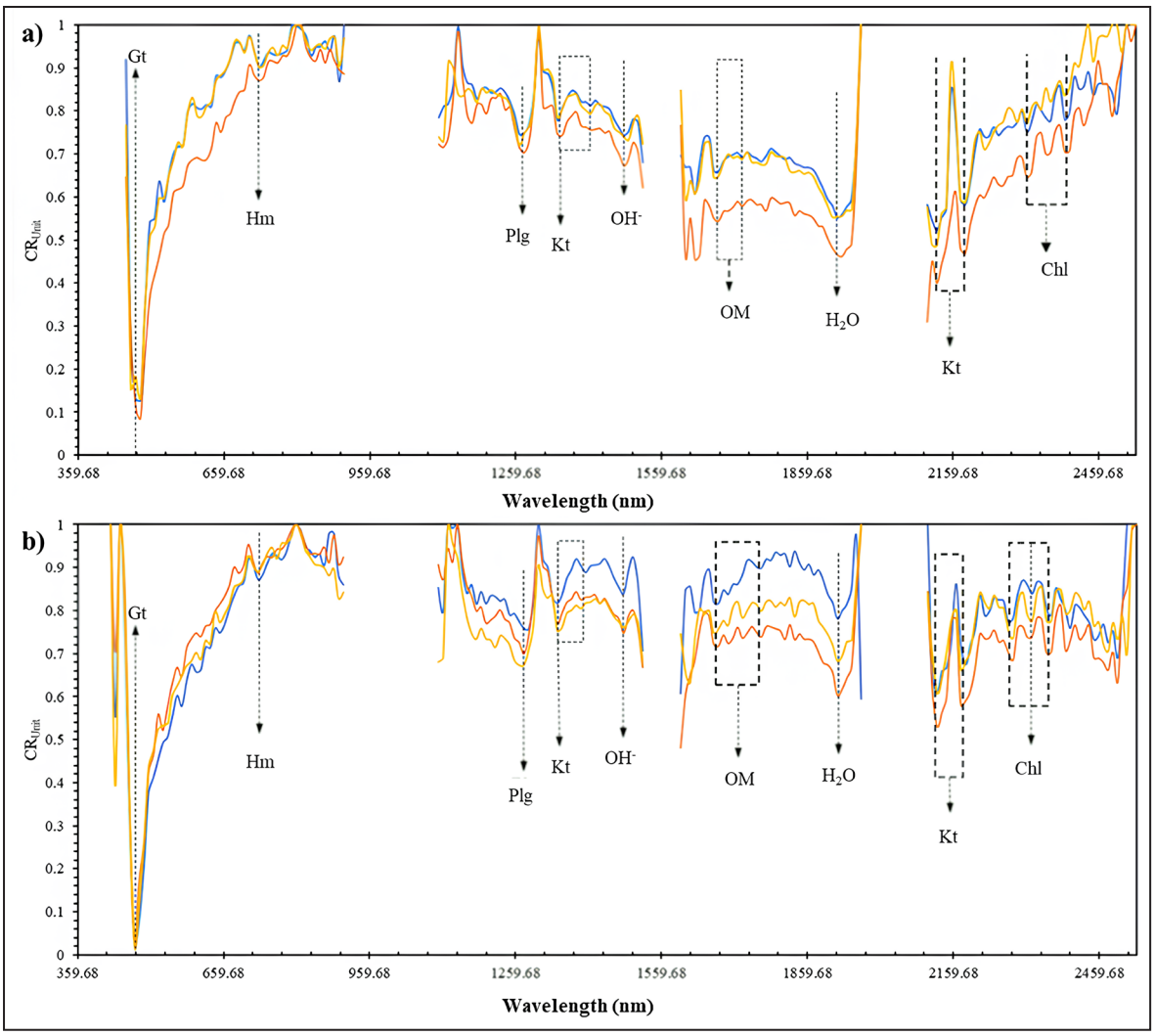

Figure 6. Mean continuum removal (CR) spectra of silty clay loam (a) and silty clay (b) which shows absorption features of minerals such as goethite (Gt), hematite (Hm), plagioclase (Plg) kaolinite (Kt), chlorite (Chl), and organic matter (OM).

processes in iron minerals (Chen *et al*., 2022b). Chen *et al*. (2022b) demonstrated that soil organic matter could significantly modulate the redox behaviour of iron minerals, thereby affecting their crystallinity. They found that organic matter can either promote or inhibit the formation of crystalline phases, depending on the specific redox conditions and interactions with iron.

Soil moisture also played a key role in the formation of these iron oxide minerals. Higher temperatures and lower humidity favoured the dehydration process, promoting hematite formation (Schwertmann, 1985). Additionally, soil pH significantly influenced hematite precipitation from ferrihydrite. Hematite transformation occured within pH ranges of 2 - 5 and 7 - 9 (Chen *et al*., 2022a). These pH-dependent changes may explain the variations in hematite observed in the different soil textures.

Plagioclase and Its Spectral Variations

Plagioclase was identified at 1,267.36 nm in silty clay and at 1,277.22 nm in silty clay loam. The shift to a longer wavelength in silty clay loam is attributed to a higher Fe content within the plagioclase structure. Serventi *et al*. (2013) demonstrated that increased Fe content shifts plagioclase absorption minima to longer wavelengths (1260 - 1270 nm), a phenomenon which is also observed in the spectral data. Sadrian *et*

al. (2023) also explained that the shifts in spectral absorption are due to changes in the crystal field environment around the Fe ions, which alter the energy levels of electronic transitions.

Chlorite Variability and Fe Content

Chlorite absorption features were observed at different wavelengths in the two textures. In silty clay, chlorite absorption appears at 2,311.68 nm, 2,360.48 nm, and 2,399.52 nm, while in silty clay loam, it is detected at 2,282.40 nm, 2,321.44 nm, and 2,360.48 nm. The shift to longer wavelengths in silty clay indicates a higher Fe content in chlorite. This aligned with findings from Yang *et al*. (2018), who reported that Fe-rich chlorite exhibits spectral absorption at longer wavelengths compared to Mg-rich varieties. Based on the observed spectral features, the chlorite present in both soil textures can be classified as chamosite, the Fe-rich variety of chlorite. Abweny *et al*. (2016) identified Mg-OH absorption in clinochlore at 2,245 - 2,325 nm and Fe-OH absorption in chamosite at 2,261 - 2,355 nm, supporting the classification.

The presence of chlorite in the soil suggests that the parent material has not undergone intensive weathering. Chlorite is a primary mineral in soils, with minor proportions derived from igneous, metamorphic, and sedimentary rocks (Schulze, 2002). In volcanic environments, chlorite can originate from hydrothermal alteration of igneous and pyroclastic rocks. Utoyo (2007) identified a chloritization alteration zone in andesitic rocks around The Cupunagara Caldera, located east of the studied area, supporting the hypothesis that the chlorite detected in this study may have been inherited from hydrothermal processes.

Kaolinite Identification in SWIR Spectra

Kaolinite absorption features were identified in paired diagnostic bands at 1,355.2 - 1,413.76 nm and 2,126.24 - 2,184.8 nm in silty clay, and at 1,345.44 - 1,404 nm and 2,126.24 - 2,175.04 nm in silty clay loam. These absorption features correspond to hydroxyl (O-H) stretching and bending vibrations, characteristic of kaolinite (García-Vicente *et al*., 2021). The presence of these absorption bands in the SWIR region (1,000 - 2,700 nm) confirms the hydroxyl-rich nature of kaolinite. Similar findings were reported by Mañosa *et al*. (2023), who described these diagnostic bands as key indicators of kaolinite presence. The absorption features around 2,200 nm result from Al-OH bending, while those at 1,400 nm correspond to Al_2OH stretching (Bishop *et al*., 2017).

Soil Mineral Identification from XRD Pattern

The results of XRD analysis showed the presence of kaolinite diffraction peaks from the texture observed at d-spacings of 4.31 Å, 3.86 Å, 3.84 Å, 2.78 Å, and 1.93 Å. as well as chlorite (Chl) at 4. 64 Å, 4.62 Å, 3.48 Å, 3.47 Å, 2.69 Å, 2.68 Å in the surface soil layer of Andisols with silty clay texture (Figure 7a) and silty clay loam (Figure 7b). Significant differences between mineral identification using spectral and XRD is that spectral methods could identify another type of mineral such as goethite, hematite, and plagioclase. This difference is due to XRD method requires iron removal before samples were tested.

Quantification of Identified Soil Minerals

Figure 8 shows that the silty clay and silty clay loam textures in the studied area contain four main minerals namely goethite (Gt), hematite (Hm), kaolinite (Kt), and chlorite (Chl). In general, goethite has a larger amplitude than hematite. The largest spectral absorption amplitude of phyllosilicate minerals was observed in kaolinite compared to chlorite. The greater the spectral absorption amplitude, the higher the percentage of the mineral present.

The difference in spectral absorption amplitude of goethite and hematite minerals depended on the type of soil texture, silty clay (Figure 8a), or silty clay loam (Figure 8b). In the silty clay, goethite showed a spectral absorption amplitude between 447.52 nm to 457.28 nm, while in the silty clay loam, the range was 447.52 nm to 467.04 nm. The absorption difference between the minimum and maximum values of goethite was 0.56 in silty clay and 0.27 in silty clay loam. Hematite, in the silty clay, showed an absorption range between 750.08

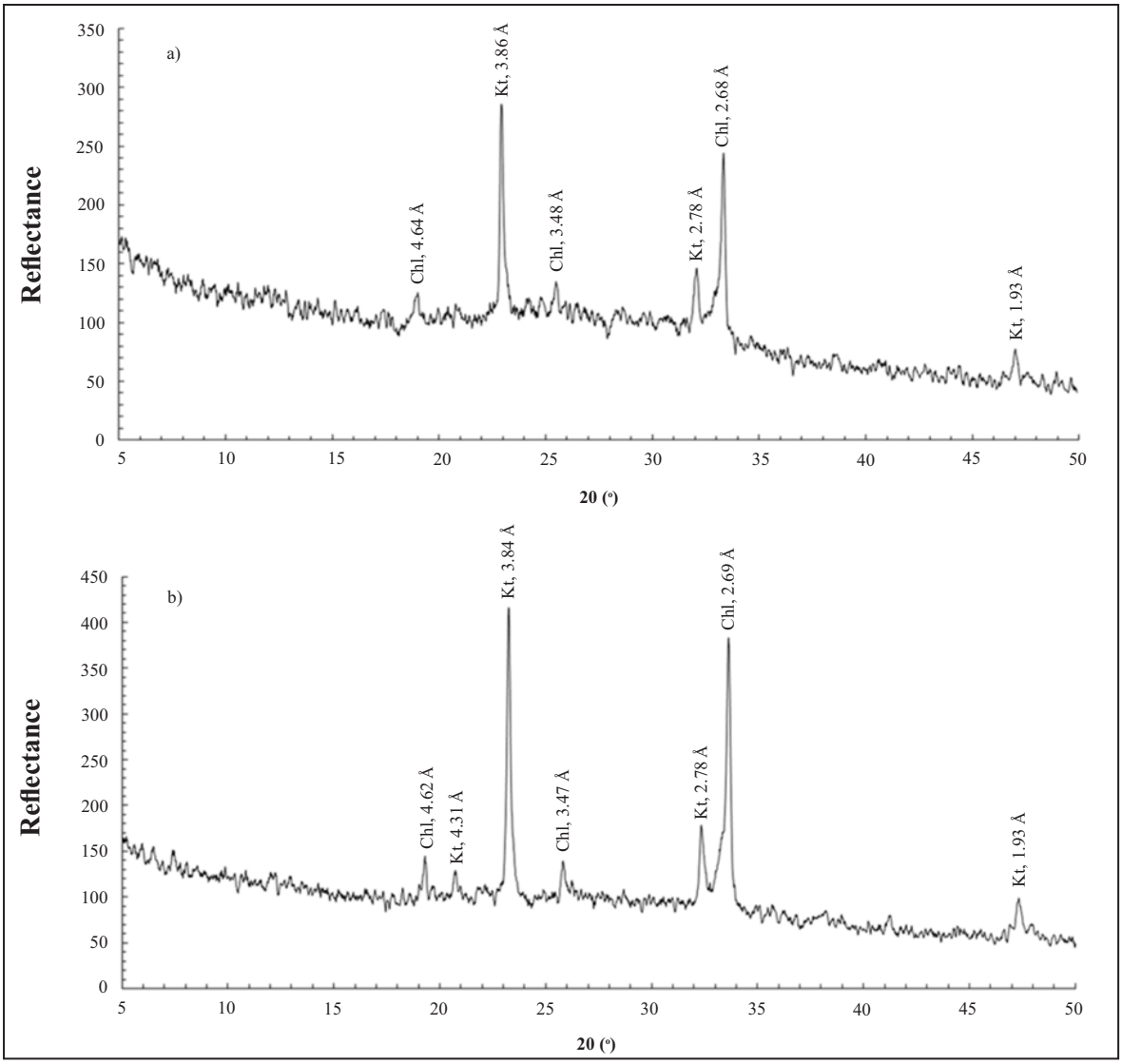

Figure 7. Diffraction peaks of kaolinite (Kt) and chlorite (Chl) from Andisols **with silty clay (a) and silty clay loam (b) textures.**

nm to 759.84 nm, with an absorption difference of 0.08. In the silty clay loam, the absorption range of hematite was 720.8 nm to 750.08 nm, with an amplitude difference of 0.14.

Kaolinite (Kt) and chlorite (Chl) had spectral absorption amplitudes in the SWIR spectral range in both soil textures (Figure 6). In the silty clay texture, kaolinite had an amplitude range from 2,155.5 nm to 2,165.3 nm, while in the silty clay loam texture it was observed having a range from 2,136 nm to 2,155.2 nm. The difference in kaolinite spectral absorption amplitude between its minimum and maximum values was 1.72 in silty clay and 1.55 in silty clay loam. Chlorite had spectral absorption amplitudes at longer wavelengths of 2,292.2 - 2,311.7 nm in the silty clay texture and 2,272.64 - 2,292.16 nm in the silty clay loam texture with amplitude differences of 0.30 and 0.58, respectively.

In general, the amplitude range of spectral absorption of the two iron oxide minerals was like the absorption spectra in previous studies from Bahia *et al*. (2015) and Stenberg *et al*. (2010). The comparison showed that goethite was more dominant in silty clay (21.03 %) and silty clay loam (12.82 %) (Table 2). Meanwhile, the proportion of hematite was higher in the silty clay loam compared to the silty clay (6.80 % vs. 3.00 %).

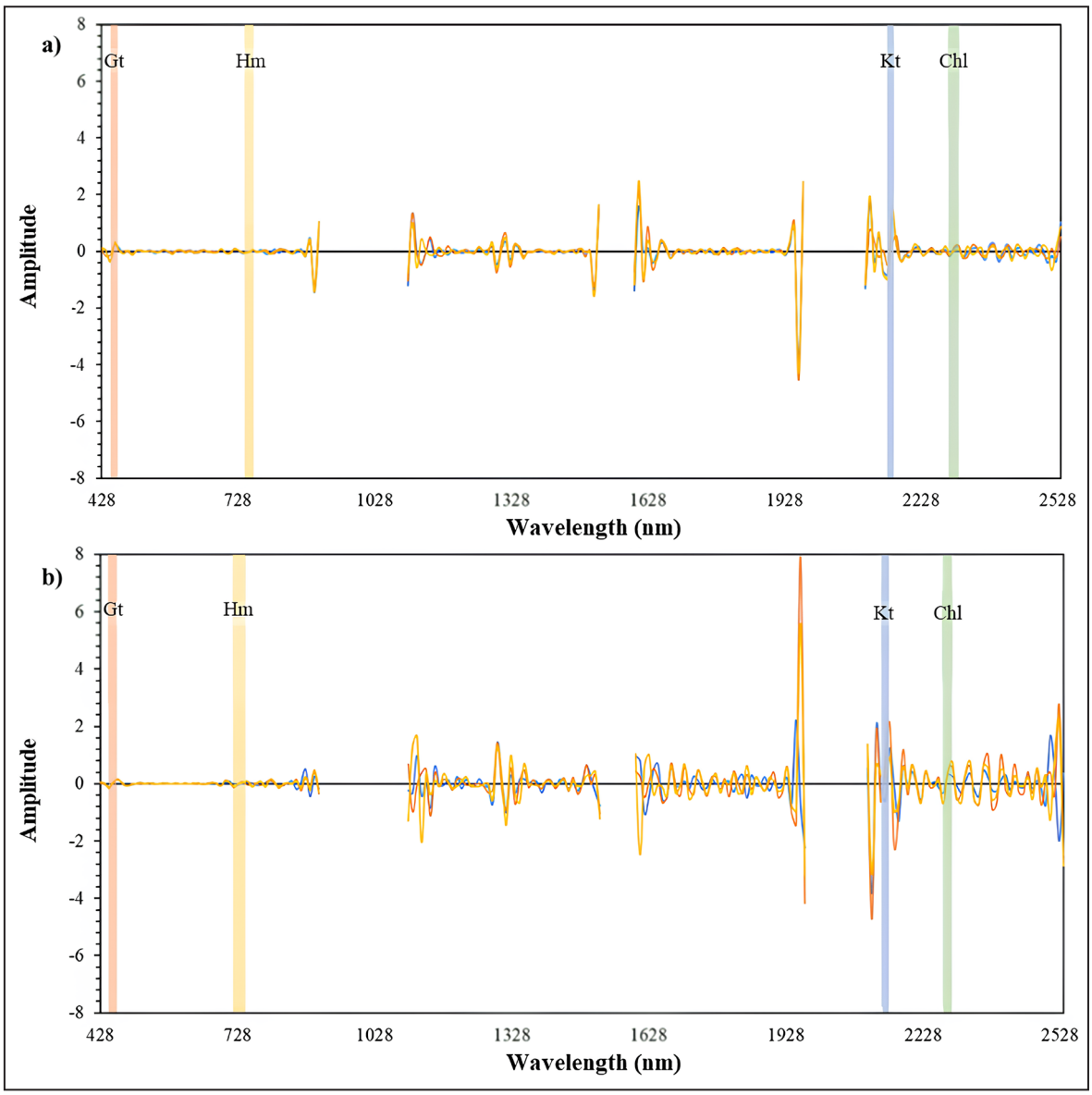

Figure 8. Amplitude of spectral absorption resulting from the application of the second derivative function and Savitzky-Golay filter of goethite (Gt), hematite (Hm), kaolinite (Kt) and chlorite (Chl) in silty clay textures (a) and silty clay loam (b).

Table 2. Quantification of Clay Minerals and Iron Oxides from Spectral Absorption

Soil Texture Class	Goethite	Hematite	Kaolinite	Chlorite
	----------%----------			
Silty Clay	21.03	3.00	64.57	11.40
Silty Clay Loam	10.67	5.66	61.00	22.68

Based on the calculation of the relative composition of kaolinite and chlorite from the amplitude, soils with a silty clay texture had higher kaolinite content (64.57 %) compared to silty clay loam (61.00 %). In contrast, chlorite in silty clay loam texture had a higher proportion (22.68 %) compared to silty clay (11.40 %). Similar relative proportions were also observed in the XRD peak curves for silty clay and silty clay loam textures showing that kaolinite compositions of 95.10 % and 21.00 %, respectively, and chlorite of 4.90 % and 89.00 %, respectively (Table 3). Quantita-

Table 3. Quantification of Clay Minerals Identified from XRD Analysis

Soil Texture Class	Kaolinite	Chlorite
	----------%----------	
Silty Clay	95.10	4.90
Silty Clay Loam	21.00	79.00

tively, the approach also aligns with earlier work showing excellent agreement between spectral data and XRD mineralogy. Omran (2017) used Hyperion imagery, and found that the soil minerals inferred from spectral unmixing were in close concordance with XRD results. Similarly, Brown *et al*. (2006) demonstrated that VNIR reflectance could predict kaolinite and montmorillonite abundances with ~96 % of samples within one ordinal unit of XRD reference values.

Although the clay mineral proportions quantified from soil spectra resemble the XRD results, the method still shows a significant disparity compared to XRD quantification. This difference arises from the complex mix of minerals and other soil substances recorded in the spectra (Ma *et al*., 2024). In this case, the XRD analysis required pre-removal of iron oxides, meaning goethite/hematite did not appear in the XRD results, whereas the spectra clearly detected them. Such sample treatments and the fact that hyperspectral data sample only the surface (0 - 5 cm) can lead to mismatches with bulk (0 - 30 cm) XRD quantification. Previous studies likewise noted that spectral data might record phases or mixtures (including hydration states and trace organics) that differ from laboratory XRD mineralogy (Kyziol-Komosinska *et al.*, 2024). Furthermore, the relatively small number of sampling locations may limit the statistical robustness and spatial representativeness of the mineral quantification results, potentially underestimating fine-scale variability within the studied area. Nevertheless, despite this limitation, the findings of this study provide valuable updated information by confirming that Hyperion EO-1 can serve as an alternative tool for detecting soil minerals, including those identified by XRD as well as minerals not captured by XRD.

Conclusions

The spectral reflectance analysis using Hyperion EO-1 imagery successfully distinguished clay texture between silty clay loam and silty clay based on their spectral characteristics across VIS-NIR-SWIR wavelengths. The most significant reflectance separation was observed in the SWIR region, indicating differences in moisture content and mineral composition. The spectral absorption analysis revealed key mineralogical differences, with hematite, goethite, plagioclase, chlorite, and kaolinite identified in both soil textures, though their absorption positions varied. The XRD analysis confirmed the presence of kaolinite and chlorite, but lacked the ability to detect iron oxides due to the required iron removal process. The quantification of soil minerals showed that goethite was more dominant in silty clay, whereas hematite had a higher proportion in silty clay loam. These findings highlighted the potential of hyperspectral remote sensing for soil mineralogical analysis, providing a nondestructive approach to assess soil mineral composition. Future studies should explore integrating hyperspectral and geochemical analyses to enhance soil characterization accuracy.

Acknowledgments

This research was funded by The Academic Research Grants (ALG) No. 1959/UN6.3.1/P.T.00/2021. The authors would like to thank all colleagues who provided constructive criticism during manuscript preparation. The authors also extend thanks to P.T. Perkebunan Nusantara VIII for permitting to conduct this research in their working area.

References

Abweny, M.S., Ruitenbeek, F.J.A. van, de Smeth, B., Woldai, T., Meer, F.D. van der, Cudahy, T., Zegers, T., Blom, J.K., and Thuss, B., 2016. Short-Wavelength Infrared (SWIR) spectroscopy of low-grade metamorphic volcanic rocks of the Pilbara Craton. *Journal of African Earth Sciences*, 117, p.124-134. DOI:10.1016/j.jafrearsci.2016.01.024.

Altinbas, U., Kurucu, Y., Bolca, M., and El-Nahry, A., 2005. Using advanced spectral analyses techniques as possible means of identifying clay minerals. *Turkish journal of agriculture and forestry*, 29 (1), p.19-28.

ASTM, 2023. Standard Guide for Forensic Analysis of Geological Materials by Powder X-Ray Diffraction. In *ASTM E3294-22*.

Bahia, A.S.R. de Souza, Marques Jr, J., and Siqueira, D.S., 2015. Procedures using diffuse reflectance spectroscopy for estimating hematite and goethite in Oxisols of São Paulo, Brazil. *Geoderma regional,* 5, p.150-156. https://doi.org/10.1016/j.geodrs.2015.04.006

Bellinaso, H., Silvero, N.E.Q., Ruiz, L.F.C., Accorsi Amorim, M.T., Rosin, N.A., Mendes, W.d.S., Sousa, G.P.B.d., Sepulveda, L.M.A., Queiroz, L.G.d., Nanni, M.R., and Demattê, J.A.M., 2021. Clay content prediction using spectra data collected from the ground to space platforms in a smallholder tropical area. *Geoderma*, 399, 115116. DOI:10.1016/j.geoderma.2021.115116.

Ben-Dor, E. 2002. Quantitative remote sensing of soil properties. *Advances in Agronomy,* 75, p.173-243. Academic Press. DOI:10.1016/S0065-2113(02)75005-0.

Bhat, M.A., Mishra, A.K., Shah, S.N., Bhat, M.A., Jan, S., Rahman, S., Baek, K.H., and Jan, A.T., 2024. Soil and Mineral Nutrients in Plant Health: A Prospective Study of Iron and Phosphorus in the Growth and Development of Plants. *Current Issues in Molecular Biology*, 46 (6), p.5194-5222. DOI:10.3390/cimb46060312.

Bishop, J.L., Michalski, J.R., and Carter, J., 2017. Chapter 14 - Remote Detection of Clay Minerals. In: Gates, W.P., Kloprogge, J.T., Madejová, J., and Bergaya, F. (eds.), *Developments in Clay Science,* 8, p. 482-514. Elsevier. DOI:10.1016/B978-0-08-100355-8.00014-X.

Brindley, G.W. and Brown, G., 1980. *Crystal Structures of Clay Minerals and their X-Ray Identification*. Mineralogical Society of Great Britain and Ireland. DOI:10.1180/mono-5.

Brown, D.J., Shepherd, K.D., Walsh, M.G., Mays, M.D., and Reinsch, T.G., 2006. Global soil characterization with VNIR diffuse reflectance spectroscopy. *Geoderma*, 132 (3-4), p.273-290. DOI:10.1016/j.geoderma.2005.04.025.

Brus, D.J., 2019. Sampling for digital soil mapping: A tutorial supported by R scripts. *Geoderma*, 338, p.464-480. DOI:10.1016/j.geoderma.2018.07.036.

Buddenbaum, H. and Steffens, M., 2012. The Effects of Spectral Pretreatments on Chemometric Analyses of Soil Profiles Using Laboratory Imaging Spectroscopy. *Applied and Environmental Soil Science*, (1), 274903. DOI:10.1155/2012/274903.

Chen, S.A., Heaney, P.J., Post, J.E., Eng, P.J., and Stubbs, J.E., 2022a. Hematite-goethite ratios at pH 2-13 and 25-170 °C: A time-resolved synchrotron X-ray diffraction study. *Chemical Geology*, 606, 120995. DOI:10.1016/j.chemgeo.2022.120995.

Chen, Y., Ma, L., Yu, D., Zhang, H., Feng, K., Wang, X., and Song, J., 2022b. Comparison of feature selection methods for mapping soil organic matter in subtropical restored forests. *Ecological Indicators*, 135, 108545. DOI:10.1016/ j.ecolind.2022.108545.

Churchman, G.J., 2018. Game Changer in Soil Science. Functional role of clay minerals in soil. *Journal of Plant Nutrition and Soil Science*, 181 (1), p.99-103. DOI:10.1002/jpln.201700605.

Clark, R.N. and Roush, T.L., 1984. Reflectance spectroscopy: Quantitative analysis techniques for remote sensing applications. *Journal of Geophysical Research: Solid Earth*, 89 (B7), p.6329-6340. DOI:10.1029/JB089iB07p06329 .

Demattê, J.A.M., Bellinaso, H., Araújo, S.R., Rizzo, R., and Souza, A.B., 2016. Spectral regionalization of tropical soils in the estimation of soil attributes. *Revista Ciência Agronômica*, 47.

de Souza Bahia, A.S.R., Marques Jr, J., and Siqueira, D.S., 2015. Procedures using diffuse reflectance spectroscopy for estimating hematite and goethite in Oxisols of São Paulo, Brazil. *Geoderma regional,* 5, p.150-156. DOI:10.1016/j.geodrs.2015.04.006

Doebelin, N. and Kleeberg, R., 2015. Profex: a graphical user interface for the Rietveld refinement program BGMN. *Applied Crystallography*, 48 (5), p.1573-1580. DOI:10.1107/S1600576715014685.

Ducasse, E., Adeline, K., Hohmann, A., Achard, V., Bourguignon, A., Grandjean, G., and Briottet, X., 2024. Mapping of Clay Montmorillonite Abundance in Agricultural Fields Using Unmixing Methods at Centimeter Scale Hyperspectral Images. *Remote Sensing*, 16 (17), 3211. DOI:10.3390/rs16173211.

Elias, M., Chartier, C., Prévot, G., Garay, H., and Vignaud, C., 2006. The colour of ochres explained by their composition. *Materials Science and Engineering: B*, 127 (1), p.70-80. DOI:10.1016/j.mseb.2005.09.061.

Fang, Q., Hong, H., Zhao, L., Kukolich, S., Yin, K., and Wang, C., 2018. Visible and Near-Infrared Reflectance Spectroscopy for Investigating Soil Mineralogy: A Review. *Journal of Spectroscopy*, (1), 3168974. DOI:10.1155/2018/3168974.

García-Vicente, A., Lorenzo, A., Morales, J., García-Romero, E., and Suárez, M., 2021. Field Spectroscopy Applied to the Kaolinite Polytypes Identification. *Environmental Sciences Proceedings*, 6 (1), 16.pp DOI:10.3390/iecms2021-09353.

Garfagnoli, F., Ciampalini, A., Moretti, S., Chiarantini, L., and Vettori, S., 2013. Quantitative mapping of clay minerals using airborne imaging spectroscopy: new data on Mugello (Italy) from SIM-GA prototypal sensor. *European Journal of Remote Sensing*, 46 (1), p.1-17.

He, L., Zhou, Y., and Zhang, C., 2024. Application of Target Detection Based on Deep Learning in Intelligent Mineral Identification. *Minerals*, 14 (9), 873. DOI:10.3390/min14090873.

Hendricks, S.B. and Fry, W.H., 1930. The results of X-Ray and microscopical examinations of soil colloids. *Soil Science*, 29 (6), p.457-480.

Kitagawa, Y., Imoto, H., and Kurihara, H., 2004. Clay mineralogy of a podzol developed under a Sciadopitys verticillata forest on Mt. Irazu, Shikoku mountains, Southwest Japan. *Soil Science and Plant Nutrition*, 50 (3), p.331-338. DOI:10.1080/00380768.2004.10408486.

Kokaly, R.F., Clark, R.N., Swayze, G.A., Livo, K.E., Hoefen, T.M., Pearson, N.C., Wise, R. A., Benzel, W., Lowers, H.A., Driscoll, R.L., and Klein, A.J., 2017. USGS Spectral Library Version 7 [Report](1035). Data Series, Issue. U. S. G. Survey. https://pubs.usgs.gov/publication/ds1035.

Kome, G.K., Enang, R.K., Tabi, F.O., and Yerima, B.P.K., 2019. Influence of clay minerals on some soil fertility attributes: a review. *Open Journal of Soil Science*, 9 (9), p.155-188. https://doi.org/10.4236/ojss.2019.99010.

Kyziol-Komosinska, J., Dzieniszewska, A., and Czupioł, J., 2024. Behavior of Silver Species in Soil: Ag Nanoparticles vs. Ionic Ag. *Molecules*, 29 (23), 5531. DOI:10.3390/molecules29235531.

Mañosa, J., la Rosa, J.C., Silvello, A., Maldonado-Alameda, A., and Chimenos, J.M., 2023. Kaolinite structural modifications induced by mechanical activation. *Applied Clay Science*, 238, 106918. DOI:10.1016/j.clay.2023.106918.

Ma, Y., Minasny, B., Roudier, P., Theng, B.K., and Carrick, S., 2024. Application of mid-infrared (MIR) spectroscopy to identify and quantify minerals in New Zealand soils. *Catena,* 242, 108115. DOI:10.1016/j.catena.2024.108115.

McAlister, J.J. and Smith, B.J., 1995. A Rapid Preparation Technique for X-Ray Diffraction Analysis of Clay Minerals in Weathered Rock Materials. *Microchemical Journal*, 52 (1), p.53-61. DOI:10.1006/mchj.1995.1066.

Mendes, W.d.S., Demattê, J.A.M., Bonfatti, B.R., Resende, M.E.B., Campos, L.R., and Costa, A.C.S. d., 2021. A novel framework to estimate soil mineralogy using soil spectroscopy. *Applied Geochemistry*, 127, 104909. DOI:10.1016/ j.apgeochem.2021.104909.

Nanni, M.R., Demattê, J.A.M., Rodrigues, M., Santos, G.L.A.A.D., Reis, A.S., Oliveira, K. M. D., and Sun, L., 2021. Mapping particle size and soil organic matter in tropical soil based on hyperspectral imaging and non-imaging sensors. *Remote Sensing*, 13 (9), 1782. DOI:10.3390/rs13091782.

Oldeman, L.R., 1975. *An agro-climatic map of Java*. In Central Research Institute for Agriculture.

Omran, E.S.E., 2017. Rapid prediction of soil mineralogy using imaging spectroscopy. *Eurasian Soil Science*, 50 (5), p.597-612. DOI:10.1134/ S106422931705012X.

Pearlman, J., Carman, S., Segal, C., Jarecke, P., Clancy, P., and Browne, W., 2001. Overview of the Hyperion imaging spectrometer for the NASA EO-1 mission. IGARSS 2001. Scanning the Present and Resolving the Future. *Proceedings IEEE 2001 International Geoscience and Remote Sensing Symposium (Cat. No. 01CH37217)*,

Pereira, G.E., Sequinatto, L., Almeida, J.A.d., ten Caten, A., and Mota, J.M., 2019. Refletância espectral VIS-NIR para discretização de solos com alto teor de areia. *Semina: Ciências Agrárias*, 40 (1), p.99-112. DOI:10.5433/1679-0359.2019v40n1p99.

Poulenard, J., Podwojewski, P., and Herbillon, A.J., 2003. Characteristics of non-allophanic Andisols with hydric properties from the Ecuadorian páramos. *Geoderma*, 117 (3), p.267-281. DOI:10.1016/S0016-7061(03)00128-9.

Priya, S. and Ghosh, R., 2024. Soil clay minerals abundance mapping using AVIRIS-NG data. *Advances in Space Research*, 73 (2), p.1360-1367. DOI:10.1016/ j.asr.2022.09.049.

Sadrian, M.R., Calvin, W.M., Perrin, A.E., Engelbrecht, J.P., and Moosmüller, H., 2023. Variations in Infrared Complex Refractive Index Spectra of Surface Soils from Global Dust Entrainment Regions. *Atmosphere*, 14 (4), 675. https://doi.org/10.3390/ atmos14040675.

Savitzky, A. and Golay, M.J.E., 1964. Smoothing and Differentiation of Data by Simplified Least Squares Procedures. *Analytical Chemistry*, 36 (8), p.1627-1639. DOI:10.1021/ ac60214a047.

Schulze, D. G., 2002. An introduction to soil mineralogy. *Soil mineralogy with environmental applications*, 7, p.1-35.

Schwertmann, U., 1985. The Effect of Pedogenic Environments on Iron Oxide Minerals. In: B.A. Stewart (ed.), *Advances in Soil Science* (p.171-200). Springer New York. DOI:10.1007/978-1-4612-5046-3_5.

Serventi, G., Carli, C., Sgavetti, M., Ciarniello, M., Capaccioni, F., and Pedrazzi, G., 2013. Spectral variability of plagioclase–mafic mixtures (1): Effects of chemistry and modal abundance in reflectance spectra of rocks and mineral mixtures. *Icarus*, 226 (1), p.282-298. DOI:10.1016/j.icarus.2013.05.041.

Silitonga, P.A., 1973. *Geological Map of Bandung Quadrangle Scale 1:100,000*. Centre for Geological Survey, Bandung.

Stenberg, B., Rossel, R.A.V., Mouazen, A. M., and Wetterlind, J., 2010. Visible and near infrared spectroscopy in soil science. *Advances in agronomy*, 107, p.163-215. DOI:10.1016/ S0065-2113(10)07005-7.

Stevens, A. and Ramirez-Lopez, L., 2013. *An introduction to the prospectr package.*

Sukarman, Muslihat, L., Gani, R.A., Agian, Y., and Risalah, N., 2016. *Semi Detailed Land Map Atlas Scale 1:50,000.*

Thompson, A., Chadwick, O.A., Rancourt, D.G., and Chorover, J., 2006. Iron-oxide crystallinity increases during soil redox oscillations. *Geochimica et Cosmochimica Acta*, 70 (7), p.1710-1727. DOI:10.1016/j.gca.2005.12.005.

Utoyo, H., 2007. Alteration and mineralization of ancient caldera in Cupunagara, Subang, West Java. *Proceedings Joint Convention Bali*.

Uzarowicz, Ł., Skiba, S., Skiba, M., and Šegvić, B., 2011. Clay-Mineral Formation in Soils

Developed in the Weathering Zone of Pyrite-Bearing Schists: A Case Study from The Abandoned Pyrite Mine in Wieściszowice, Lower Silesia, SW Poland. *Clays and Clay Minerals*, 59 (6), p.581-594. DOI:10.1346/CCMN.2011.0590604.

Wadoux, A.M.J.C., Malone, B., Minasny, B., Fajardo, M., and McBratney, A.B., 2021. Pre-processing of Spectra. In *Soil Spectral Inference with R: Analysing Digital Soil Spectra using the R Programming Environment* (p.49-79). Springer International Publishing. DOI:10.1007/978-3-030-64896-1_5.

Xiao, J., Song, Y., and Li, Y., 2023. Comparison of Quantitative X-ray Diffraction Mineral Analysis Methods. *Minerals*, 13 (4), 566. DOI:10.3390/min13040566.

Xing, B. and Dudas, M.J., 1994. Characterization of Clay Minerals in White Clay Soils, People's Republic of China. *Soil Science Society of America Journal*, *58 (4)*, p.1253-1259. DOI:10.2136/sssaj1994.03615995005800040037x.

Yang, M., Ye, M., Han, H., Ren, G., Han, L., and Zhang, Z. 2,018. Near-Infrared Spectroscopic Study of Chlorite Minerals. *Journal of Spectroscopy*, 2018 (1), 6958260. DOI:10.1155/2018/6958260.

Zhang, Y.w., Wang, K.b., Wang, J., Liu, C., and Shangguan, Z.p., 2021. Changes in soil water holding capacity and water availability following vegetation restoration on the Chinese Loess Plateau. *Scientific Reports*, 11 (1), 9692. DOI:10.1038/s41598-021-88914-0.